

# Experimental verification of the IPI sizing technique

Sebastian Kosch, University of Toronto

July 2014



# List of symbols and abbreviations

$\Delta\vartheta$	Angular spacing between two adjacent fringes
$\Delta z$	Distance along the $z$ -axis between the focal plane of the lens and the light sheet
$\hat{N}_{\text{fr}}$	Peak fringe count measured
$\kappa$	Scalar value relating the fringe count $N_{\text{fr}}$ to the physical diameter of the particle $D_d$
$D_i$	Diameter (in pixels) of the defocussed image
$D_{\text{padded}}$	Width (in pixels) of the padded input to the Fourier transform
$D_d$	Physical diameter of the particle (here: droplet)
$d_{p,x}; d_{p,y}$	Physical dimensions of a pixel on the camera's CCD sensor
$f_{\text{peak}}$	Peak frequency
$M$	Magnification
$N_{\text{fr}}$	Number of fringes
$s_x$	Distance, in pixels, between two adjacent fringes



# **Introduction**

## **1.1 Why spray sizing is important**

## **1.2 What our contributions in this paper are**

- Our contributions:
  - Pupillary magnification has to be taken into account
  - Circle detection algorithm is crap

## **1.3 What other work has been done in this area**



# Experimental setup

- What kinds of setups there are
  - Our setup:

## 2.1 Dantec system

- Dantec system

## 2.2 PDPA system

- TSI system



# Monodisperse droplet generation

To calibrate any droplet sizing device, we need droplets of known and uniform size. Sprays or streams of such uniform droplets are called *monodisperse*, and many different varying approaches to generating them have been proposed, each one with advantages and drawbacks.

The most basic type of droplet generator is a capillary tube, for instance a hypodermic needle or a pulled glass pipette. Droplets are generated as the liquid flows through the tube due to its own weight. As the liquid leaves the tube, it wets the tip of the tube and forms a bead held together by surface tension. Eventually, the bead's gravitational forces overcome the attraction to the tube surface, and the drop separates from the tube.

Given a liquid and its physical properties, the only remaining controllable variable is the diameter of the capillary tube tip. As a rule, droplets generated in this fashion will be significantly larger than the tube diameter from which they grow. Most droplet generators are designed to prevent this from happening:

- *Aerodynamic* droplet generators use coaxial air flow to shear the forming droplet off of the capillary tip before it can grow to full size.
- *On-demand* droplet generators use a pressure pulse to eject a fixed amount of liquid out of the capillary (or other orifice).
- *Continuous-stream* droplet generators use mechanical vibrations to break up a continuous jet of liquid emanating from the capillary into monodisperse droplets.

More exotic types of droplet generators exist: Walton and Prewett [1] suggested that water falling on spinning disks is propelled outwards, forming nearly monodisperse droplets, and several improved designs have been published since. Another approach, e.g. used by

Merritt and Drinkwater [2], involves mechanized dipping of a needle into a liquid reservoir, and then flicking it so as to produce one droplet.

### 3.1 Aerodynamic droplet generators

Allan et al. [3] provide a history of aerodynamic designs: the first design was published in 1947 by Lane [4]; Reil and Hallett [5] later improved on it by using time-controlled air pulses instead of a continuous flow. Coggins and Baker [6] have proposed a more elaborate apparatus with variable air and liquid flow and adjustable needle position.

#### 3.1.1 Stry design

Initial tests based on a design by Stry [7] showed that the ability of the instrument to produce droplets below  $600 \mu\text{m}$  depends entirely on the precision with which the flow of water and air can be controlled.

### 3.2 On-demand drop generators

Drop-on-demand technology finds its most important application in printing. Indeed, the most prominent designs representative of this category are the thermal droplet generators found in most household inkjet printers, invented by Endo et al. [8]. At least one research group, Sergeyev and Shaw [9], has succeeded in repurposing an old inkjet print head for laboratory droplet generation.

Less widespread, but more flexible in a research setting, are on-demand generators driven by the contraction of piezoelectric elements, such as those proposed by Yang et al. [10] or Ulmke et al. [11]. Excellent reviews on drop-on-demand designs were published by Le and Lee [12, 13].

A curious third type of on-demand generator by Amirzadeh Goghari and Chandra [14] uses a short pulse of pressurized air, controlled by a solenoid valve, to eject a small amount of liquid through an orifice.

While drop-on-demand generators are a crucial component in applications like inkjet printing or microfluidics, they tend to suffer from aspirated air bubbles, pileup of liquid around the nozzle tip, clogging, and other issues thwarting reliable drop expulsion unless manufactured and operated with great attention to detail.

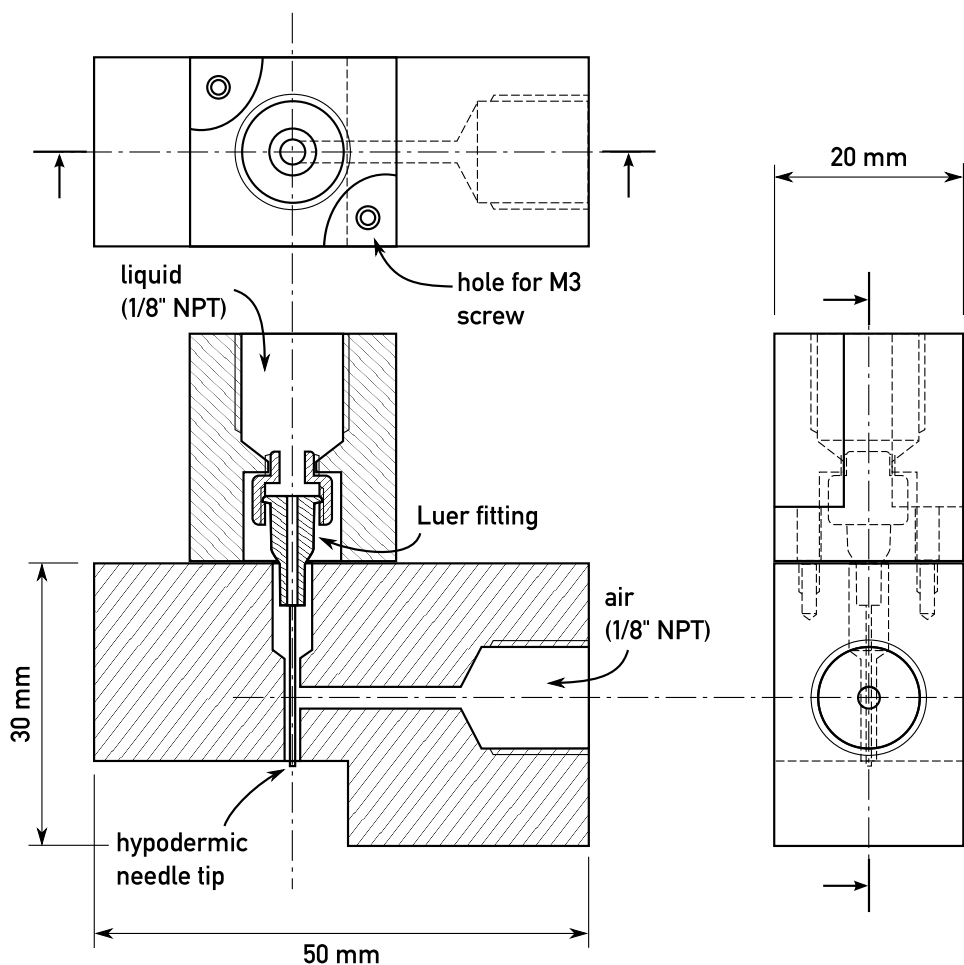


Figure 3.1: Schematic drawing of the coaxial-flow aerodynamic droplet generator, based on Stry [7]. Top: top view, right: rear view (third angle projection). Sectional view illustrates operating principle.

### 3.2.1 Amirzadeh Goghari and Chandra design

We constructed a droplet generator based on the design by Amirzadeh Goghari and Chandra [14]. While both its construction from off-the-shelf parts and its operation are remarkably straightforward, it has two limitations:

- the duration of the air pulse is limited by the response time of the solenoid valve used. The shortest pulse we were able to reliable produce was on the order of a few milliseconds, which did not permit us to produce droplets smaller than a few hundred microns in diameter, and
- the head of water over the orifice must be kept very low to prevent leakage. As a result, the number of droplets that can be ejected is limited before the water needs to be replenished.

Owed to our lack of access to an automatic micropipette puller, the nozzles used in this experiment were not optimal, which likely contributed to our experience of frequent satellite droplets and liquid buildup at the nozzle tip.

### 3.2.2 Modified Yang design

A popular piezoelectric-based drop-on-demand design was proposed by Yang et al. [10]. It consists of a liquid-filled chamber, one wall of which is the underside of a piezoelectric disk—a brass disk coated with a circular piece of piezoelectric material, commonly found in electric buzzers.

To evaluate the performance of such a drop generator, we constructed several modifications of it, the final one of which is shown in Fig. 3.2. To make the chamber as flat as possible, minimizing the distance between piezoelectric disk and orifice, it has a depth of only about 2.5 mm, the thickness of a sheet of acrylic. A second sheet holds the disk in place, while a third sheet makes up the bottom wall of the chamber. Nozzle and inlet are glued directly into the bottom sheet.

To operate the droplet generator, water is fed through the inlet port until the chamber is filled and all air bubbles have escaped through the upward-facing nozzle. The generator is then turned so that the nozzle faces down and 30 ms pulses of about 30 V are delivered to the piezoelectric disk.

The greatest challenge faced was the accumulation of liquid on the nozzle surface, which quickly led to satellite droplets or thwarted droplet production altogether. Again, capillaries drawn with an automatic pipette puller are likely more resistant to this effect.

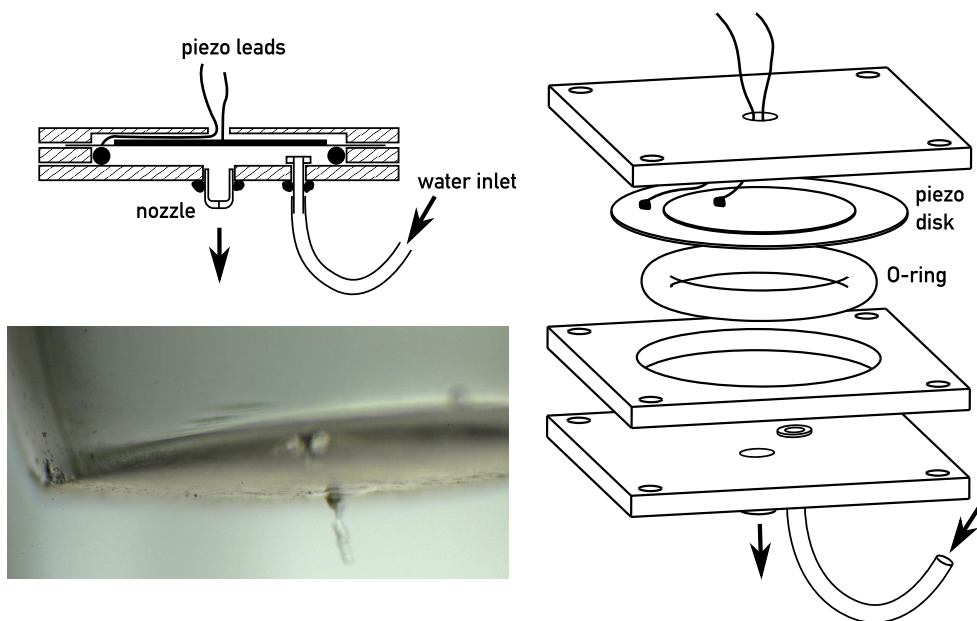


Figure 3.2: Top and right: schematic cross-section and exploded view of our piezoelectric droplet generator. Bottom left: photomicrograph of the nozzle tip ejecting a column of water (diameter  $\approx 125 \mu\text{m}$ ), which is about to coalesce into a round droplet.

### 3.2.3 Failed approaches

- Making orifices in acrylic sheets by drilling with needles (beautiful, but too large) or by poking through it with heated needles (kinda works, but the holes are super rough because hot plastics tends to bubble up and deform).

## 3.3 Continuous-stream drop generation

There exist continuous-stream drop generators based on coaxial air flow [15] and on, but most continuous-stream drop generators are based on *Rayleigh breakup*, i.e. the disintegration of a disturbed liquid jet into droplets. The physics behind this phenomenon have been studied for almost two centuries [16, 17] and are well-understood. When the jet disturbances are induced by carefully controlled mechanical vibrations at an appropriate frequency, the droplets will be of uniform size and evenly spaced.

This simple principle has been employed to generate droplets for fifty years, with orifices typically attached to either one of two vibrating mechanisms: an ordinary loudspeaker, first used by Donnelly and Glaberson [18], or a piezoelectric element, as first proposed by Schneider and Hendricks [19] and popularized by Berglund and Liu's design [20].

### 3.3.1 Hard-drive based drop generator

The accuracy of the hypodermic needle nozzle often isn't quite as good as that of e.g. photofabricated nozzles, as those have sharp edges. The round edges lead to variability in discharge coefficient (and mass flow), resulting in variance in drop volume [21]. Nevertheless, for the purpose of verifying the validity of measurements, it'll do.

Both speaker-based and piezo-based approaches have certain drawbacks: by design, a speaker vibrating at a fixed pitch produces an audible sound, jeopardizing the laboratory peace. Speakers are unshapely, difficult to fasten onto an experimental setup and their cones provide no robust structure to which any type of orifice could be attached. Piezoelectric elements cost more and are useful only when integrated with the orifice—precision machined droplet generators operating this way are commercially available, but unreasonably expensive in many situations. As a result, we felt compelled to consider alternative sources of vibration that require a minimum effort to build and install using standard lab equipment, and chose the actuator mechanism found in every magnetic hard drive for the following properties:

**Very low cost.** With high-capacity and solid-state devices rapidly pushing older hard drives into obsolescence, it should be a simple matter to acquire a few decommissioned specimens for demolition. Hard drives come in two form factors—3.5 and 2.5 inches wide, respectively—and both can be used for the purposes of this paper.

Further, glass needle orifices fabricated for use with existing loudspeaker setups can be reused, and are easily produced by hand from heated borosilicate capillaries or using a micropipette puller. The process is illustrated in FIG. 3.3 and in-depth instructions are given by Lee[13]. Piezoelectric-based devices, on the other hand, need fitted orifices to produce a range of drop sizes.

**Ease of construction and installation.** Unlike loudspeakers, hard drives have a flat base plate which can be drilled into, allowing for easy installation on any experiment jig. Save for a drill and a saw, no machining tools are needed for the construction of the droplet generator.

**High amplitudes without noise.** Like piezoelectric elements, vibrating actuator arms are very quiet, enabling use at frequencies and amplitudes that would far exceed responsible levels on a speaker. In our experiments, the actuator responded to frequencies throughout our hearing range—i.e., up to 17 kHz—and likely well beyond, though we have not tested the full response range for any given amplitude.

As an added advantage over other designs, no amplification is needed. Below 100 Hz, amplitudes on the order of 0.5 cm are easily achieved (albeit they are of course not needed for droplet production) when a peak-to-peak voltage of 2 – 4 V is applied. The amplitude scales down with the inverse of the frequency, however, such that amplitudes are much smaller at typical operating frequencies (0.5 – 10 kHz). Nevertheless, the voltages required are well within the ability of any standard laboratory function generator, and can likely even produced by many consumer-level computer sound cards.

### Operating principle

Magnetic hard drives store data as sub-micron-sized patterns of oppositely magnetized dots on disks called *platters*. The read-write head is mounted at the tip of an arm that pivots across the platter surface while the platter spins. This setup allows the head to access the entire platter surface.

FIG. 3.4 illustrates schematically the design of a typical actuator arm assembly. The flat voice coil mounted on the surface is responsible for the arm’s side-to-side movement: as it is positioned under a permanent magnet, the coil creates a sideward force when a current



Figure 3.3: Above: assembly of nozzle from low-gauge hypodermic syringe (Luer fitting) and capillary. Below: nozzle tip fabrication, capillary from left to right: broken, sanded, heated in a flame (I.D. 200  $\mu\text{m}$ ), heated for longer (I.D. 25  $\mu\text{m}$ , could be sanded down by about 200  $\mu\text{m}$ ), overheated (I.D. 0  $\mu\text{m}$ ).

flows through its wires. By stopping or reversing the current the arm's motion is likewise stopped or reversed. Since a typical hard drive's platter spins at up to 7200 RPM, actuator arms must be able to move with extreme speed and precision. They are thus engineered to be very light yet stiff. These characteristics make a magnetic hard drive's actuator arm an ideal supplier of in-plane vibrations. Indeed, hard drive actuators are remarkable not for their operating principle but for their low cost; it is only the economics of mass manufacturing that has in recent years enabled these high-speed, lightweight precision mechanisms to become so widely available.

### Construction

If possible, forgo multi-platter drives, as they are more cumbersome to disassemble and have bulky, complex actuator assemblies. The device shown in FIG. ?? is based on a single-platter drive.

**Dismantle and cut.** After removing the hard drive cover, remove the magnet holder, arm axis, arm, ribbon wires, circuit boards, and platters such that only the base plate remains. Now the corner of the base plate holding the actuator arm assembly can be cut out to yield the result shown in FIG. 3.4. A band saw, jigsaw or powered hacksaw will be very useful, although not necessary. The goal is to allow the tip of the arm to protrude over the edge.

**Expose coil leads.** Next, remove the read/write head and all wiring leading to it, along with any connected I/O and servo circuitry. Be careful, however, not to tear off the two strands powering the voice coil. If they are integrated in a ribbon you wish to remove, ensure that exposed terminals remain onto which you can solder new leads.

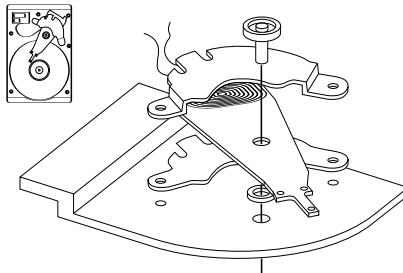


Figure 3.4: Top view of a hard drive and exploded view of the cut-out base plate, actuator arm, axis, and magnet assembly.

**Add protective cover.** We recommend bolting on a cover plate, such as a small sheet of acrylic or polycarbonate, to protect the protruding arm from accidental bending. Drill a hole through the cover to allow the nozzle to be threaded through the arm. A severable connection from coil to function generator is preferable to a direct wire, if only because the voice coil leads are delicate and easily torn off. To this end, we epoxied an audio jack into the cover and soldered the voice coil leads to it from the bottom.

### Operation

To use the droplet generator, simply insert a nozzle through a small hole at the tip of the actuator arm—typically at least one hole will already be present, but you may wish to drill more—and connect the voice coil leads to the output terminal of a function generator set to an initial peak-to-peak voltage of 1 V and a sinusoid frequency of about 50 Hz, which should cause weak but perceptible oscillations.

We used existing nozzles manufactured by hand from hypodermic needle stubs and heated glass capillaries (FIG. 3.3). We make no claim that this is the best approach to take, but we note that the interchangeability of nozzles with Luer fittings has proved very convenient in our application. How the nozzle can be held in place falls beyond the scope of this article; while we used an existing setup made from machined aluminum, a small lab stand and clamp should suffice to hold the male Luer fitting connecting the feed tube to the nozzle.

The nozzle must be supplied by an accurately calibrated syringe pump. It is convenient to integrate a large liquid reservoir (or tap water hose) via a T-valve between the pump and nozzle to permit quick topping up of the syringe. In such a setup ensure that the reservoir valve is shut closed before operation, since pressure fluctuations at the nozzle are the most common culprit for unstable jet breakup conditions.

As with other vibrating orifice droplet generators, it is crucial that stable conditions

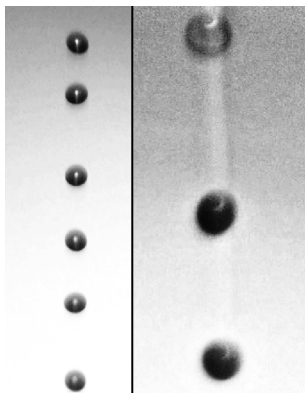


Figure 3.5: Photographs of different droplet sizes ( $220 \mu\text{m}$  and  $386 \mu\text{m}$ ,  $f = 1.990 \text{ kHz}$  and  $1.065 \text{ kHz}$  respectively) produced with the droplet generator shown in FIG. ???. Scales have been cropped out.

are established before any experiments can begin. First, confirm that the liquid is ejected in a single jet. Multiple jets can be due to a clogged orifice (a mixture of distilled water and CLR®, drawn back through a syringe, is an excellent remedy). Satellite droplets can also form secondary jets, in which case the oscillation frequency must be adjusted or the amplitude reduced. Satellite formation is easily detected by using a gentle air flow to deflect the jet—if the droplets are truly monodisperse, they will all deflect at the same angle.[22]

## 3.4 Photographic verification of droplet sizes

This is where I show pictures and tables, showing that the formula actually works.

While there are different methods of photographing droplets, just taking pictures in front of a strobe light has worked well.

### 3.4.1 Colliding droplets

No droplet generation mechanism is perfect. Small fluctuations in flow rate, unwanted harmonic vibrations and air turbulence can cause disturbances in the stream of evenly spaced droplets – the smaller the droplets, the more often this happens. Occasionally, this will lead to the collision of two droplets some distance away from the orifice.

When two drops of diameter  $D_d$  collide, the diameter of the new droplet equals

$$D_{d+d} = 2\sqrt[3]{2} \left(\frac{D_d}{2}\right)^3 = \sqrt[3]{2} D_d \approx 1.26 D_d. \quad (3.1)$$

Indeed, secondary peaks will often appear in diameter histograms at precisely 126% of the peak diameter. As long as the underlying phenomenon is understood and kept under control, these secondary peaks should be no cause for concern during the calibration. Typically, photographs will confirm that a few droplets go astray and collide with others. Since the “real” diameter peaks are easily discerned, the secondary peaks can simply be ignored.



# Interferometric Particle Imaging (IPI)

[Introductory paragraph], saying that this is also called ILIDS (invented by Glover et al. [23])

## 4.1 Operating principle

The number of fringes  $N_{\text{fr}}$  appearing in the image has a simple linear relationship to the droplet diametre  $D_d$ :

$$N_{\text{fr}} = \kappa D_d, \quad (4.1)$$

where  $\kappa$  is a constant derived from the optical configuration:

$$\kappa = \frac{\arcsin\left(\frac{D_a}{2z}\right)}{\lambda} \left( \cos\frac{\varphi}{2} - \frac{m \sin\frac{\varphi}{2}}{\sqrt{m^2 + 1 - 2m \cos\frac{\varphi}{2}}} \right). \quad (4.2)$$

In the above expression  $D_a$  is the aperture diametre,  $z$  is the distance of the lens to the laser sheet,  $\varphi$  is the off-axis angle (90 degrees in most setups, including ours), and  $m$  is the relative refractive index of the droplets (1.333 for water in air).

As a consequence of geometrical optics, the distance  $s_x$  (in pixels) between two adjacent fringes has a linear relationship with the defocussing distance  $\Delta z$ , where  $M$  is the magnification,  $d_{p,x}$  is the physical size of a camera sensor pixel, and  $\Delta\vartheta$  is the angle subtended by two adjacent fringes entering the lens [24]:

$$s_x = \frac{\Delta\vartheta \Delta z}{M d_{p,x}} \quad (4.3)$$

Of course, equation (4.3) is only meaningful where  $\Delta z \gg 0$ . If the image is (approximately) focussed, fringes will give way to a sharp image of either both glare points or a single bright spot – depending on diffraction effects and the camera’s resolution.

(Fill in more details here.)

#### 4.1.1 Influence of the scattering angle $\varphi$

The scattering angle  $\varphi$  determines the relative contribution of different scattering orders of light to the imaged fringe pattern. Both geometric optics [25] and Mie theory provide methods to compute the total scattered intensity for a given  $\varphi$  and  $m$ . Some examples can be found in Kawaguchi et al. [26] and Mounaïm-Rousselle and Pajot [27]. The geometric analysis approach is not valid beyond  $\varphi > 70^\circ$ , as the first-order scattered beam ( $p = 1$ ) is not visible from this angle [23].

While authors have identified several forward angles as optimal for their applications, e.g.  $\varphi = 45^\circ$  [23] or  $\varphi = 66^\circ$  [27], such configurations inevitably result in a variation in  $z$ , leading to different degrees of defocussing across the image – unless the camera itself is angled with respect to the lens to correct for this aberration (the so-called *Scheimpflug condition*). Since the latter approach requires specialized optical equipment,  $\varphi = 90^\circ$  is used in many setups, including the one in this paper (Section 4.2).

#### 4.1.2 Optical limits on fringe detection

Optics impose theoretical and practical size limits on the droplets to be measured. We will outline them in the following paragraphs; the reader is referred to Damaschke et al. [28] for a more detailed analysis.

**Nyquist criterion for the fringe density.** The Nyquist criterion requires that for the camera to be able to resolve a pair of neighbouring fringes, they must be at least two pixels apart. This can easily be achieved by sufficiently defocussing the lens, which widens the fringe image, increasing the number of pixels covered by each fringe. The lens mechanics permitting, any arbitrarily large droplet can thus be measured after a quick adjustment. In theory, this correction is effective until the defocussed droplet image is too large for the CCD sensor, and fringes are cut off. In practice, overlap and noise (see below) will cause significant problems long before the image can be defocussed beyond the sensor edges.

**Overlapping droplet images.** As the lens is brought farther out of focus, the droplet images dilate and overlap one another. Increasing levels of overlap frustrate attempts to iden-

tify and analyse the images. Although the slit aperture method discussed in Chapter 5 was developed to circumvent this effect, it is not entirely immune to it – particularly when droplets are very closely spaced, as they often are when vibrating orifice droplet generators are used. See Section 4.3.1 for a more in-depth discussion.

**Signal-to-noise ratio.** Image noise is a significant source of trouble in IPI analysis – indeed, many droplet images must be discarded as data sources because they are too noisy. Noise affects small droplets in particular because they scatter less light than larger ones,<sup>1</sup> but it is also a problem with deeply out-of-focus images of very large droplets, as dilated droplet images spread the same amount of light over a greater area on the camera sensor. As a result, they are darker on average than less defocussed images.

**Minimum droplet size.** Damaschke et al. [28] argue that the smallest measurable droplet is one that produces exactly one fringe covered by the aperture. We propose that, at least in theory, a partial fringe should be measurable if its image is sufficiently zero-padded before the Fourier transform is applied to it. *This might need elaboration.* In practice, the intensity of scattered light is likely to drop below an acceptable level before the fringes become too large, and noise (see above) will become the overwhelming problem. The researcher should also be aware that the assumptions of geometric optics that underlie (4.2) do not hold for small droplets (see Section 4.3.3 for details).

## 4.2 Setup

(How it's set up, what cameras, what lenses, what laser, timer box, software, etc.)

## 4.3 Common problems and sources of error

### 4.3.1 Too much overlap

This is a section where I refer to the paper that calculates overlap probabilities/overlap coefficients. I explain that many droplets are mis-identified (either high-freq is seen as low-freq, or noise is seen as high-freq) and where I point out that while Hanning windows and min-distance/max-overlap filters help a little bit, they also skew the representativeness of the sample because only small, dispersed satellites are outside of the main flow.

---

<sup>1</sup>The scattered intensity grows with the cross-section of the droplet

I explain that there isn't really an easy method of fixing this, and that any time spent attempting to deal with the problem is better spent building a slit aperture system, as described in the next chapter.

#### 4.3.2 Thin lens assumption

What matters is the Numerical Aperture (NA), which is (the sine of half of) the collection angle. When we have a simple lens, we can calculate this as

$$\text{NA} = \sin \frac{d_a}{2z} 3\alpha\rho = \sqrt{2\lambda xr} \quad (4.4)$$

The Dantec manual suggests using the distance from light sheet to front of the lens for  $z$ , and the ratio of min focal length and max f-number to find  $d_a$ . This, however, does not result in an accurate value for the collection angle with all lenses.

We are assuming, then, that the effective aperture (the entrance pupil) always stays constant throughout the focussing range of the lens. This is not necessarily the case, as there are lenses which change both the physical and the virtual size of the aperture when focussing. The best way to get the collecting angle is to go by magnification

Here is where I make the claim that it is impossible to determine the actual exact value for the numerical aperture of the lens. Similarly, it can be quite difficult to determine the accurate distance from light sheet to lens aperture (even though the latter measurement is more forgiving, since the distances are far greater).

#### 4.3.3 Error in the Mie approximation at small sizes

As outlined in paper ... geometric optics deviate from the true Mie scattering field when sizes are very small.

#### 4.3.4 Centre discrepancies

The most challenging stage of the measurement process is the detection of the defocussed droplet images. Since the defocussed images assume the shape of the aperture, which is wide open in most applications,<sup>2</sup> they are typically circular. Moreover, they are all more or less of the same size as a consequence of equation (??).

---

<sup>2</sup>see Chapter ?? for a discussion of the benefits of non-circular apertures.

Figure 4.1: Overlapping defocussed droplet images

## 4.4 Eliminating centre discrepancies and the need for camera calibration

It thus stands to reason that a simple circle detection technique would suffice to detect the droplet images in the photos. A polar adaptation of the Hough accumulator technique (such as the OpenCV implementation `cv2.HoughCircles()`) or a correlation-based pattern matching method (e.g. `cv2.matchTemplate()`) are both obvious choices for this task. The problem of *droplet overlap*, however, can thwart such efforts (Figure 4.1). This happens particularly when large droplets are to be measured, because their many fringes require larger defocussed images to resolve clearly. Indeed, in regions of high droplet density, it can be impossible to reliably detect the circular fringe images using the methods mentioned above.

Nevertheless, once droplet image positions are established with confidence, overlap can be dealt with to a degree: known overlapping regions can either be excluded entirely or serve to help find maximum-likelihood frequency peaks for their respective tributary droplet images.

Since the detection of droplet images is so essential, the Dantec DynamicStudio software extracts the droplets' positions from the focussed photo, and then maps those positions onto the defocussed photo based on a set of camera calibration photos. This method is sound in principle, but often yields unsatisfactory mappings in practice, likely whenever the calibration target plate (Figure ??) is not precisely aligned with the laser sheet. In Section ??, we describe a more accurate and robust method of finding the mapping based directly on the pair of droplet photos.

Since the mapping error is often a perspectivity, the simple manual  $x/y$ -shift that can be applied in the DynamicStudio software after calibration is not a sufficient adjustment.

Dantec supplies a *standard dot target*, a white  $10 \times 10 \text{ cm}^2$  plate engraved with a pattern of black dots (Figure ??). The plate is to be mounted such that its surface coincides perfectly with the laser sheet. Both cameras are then focussed on the dot pattern, and a photo is taken with both. This allows the DynamicStudio software to calculate the transformation matrix

between target plate and image for each camera:

$$\begin{bmatrix} x' \\ y' \\ z' \\ r' \end{bmatrix} = \begin{bmatrix} S_x & A_{yx} & A_{zx} & T_x \\ A_{xy} & S_y & A_{zy} & T_y \\ A_{xz} & A_{xy} & S_z & T_z \\ P_x & P_y & P_z & S_0 \end{bmatrix} \begin{bmatrix} x \\ y \\ z \\ 1 \end{bmatrix}. \quad (4.5)$$

In practice,  $P_{x,y,z} = 0$  and  $S_z = S_0 = 1$ , such that the mapping is affine (although we will later show that this need not be the case). The  $z$ -components (third row/column) are ignored, such that a  $3 \times 3$  matrix suffices for the purposes of this discussion:

$$\begin{bmatrix} x' \\ y' \\ r' \end{bmatrix} = \begin{bmatrix} S_x & A_{yx} & T_x \\ A_{xy} & S_y & T_y \\ P_x & P_y & S_0 \end{bmatrix} \begin{bmatrix} x \\ y \\ 1 \end{bmatrix}. \quad (4.6)$$

The DynamicStudio software thus finds the camera matrices  $\mathbf{P}_{\text{foc}}$  and  $\mathbf{P}_{\text{def}}$  mapping the object (the target plate) onto the two camera images:<sup>3</sup>

$$\mathbf{x}'_{\text{foc}} = \mathbf{P}_{\text{foc}} \mathbf{x} \quad (4.7)$$

$$\mathbf{x}'_{\text{def}} = \mathbf{P}_{\text{def}} \mathbf{x}. \quad (4.8)$$

It follows that the quotient of the two matrices, also known as the homography

$$\mathbf{H} = \mathbf{P}_{\text{def}} \mathbf{P}_{\text{foc}} \quad (4.9)$$

can be used to map the focussed image onto the defocussed image:

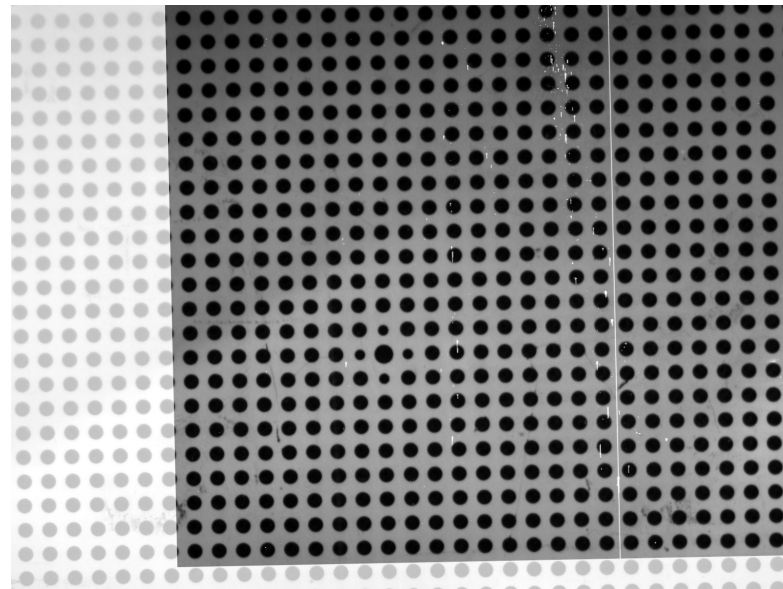
$$\mathbf{H} \mathbf{x}'_{\text{foc}} = \mathbf{x}'_{\text{def}}. \quad (4.10)$$

In practice, it is not always possible to ensure that the dot target plate is aligned with the laser light sheet to absolute perfection. This introduces a perspective error in the homography matrix  $\mathbf{H}$ . Figure 4.2a shows that even though the calibration images are mapped perfectly, there is a perspective error in Figure 4.2b.

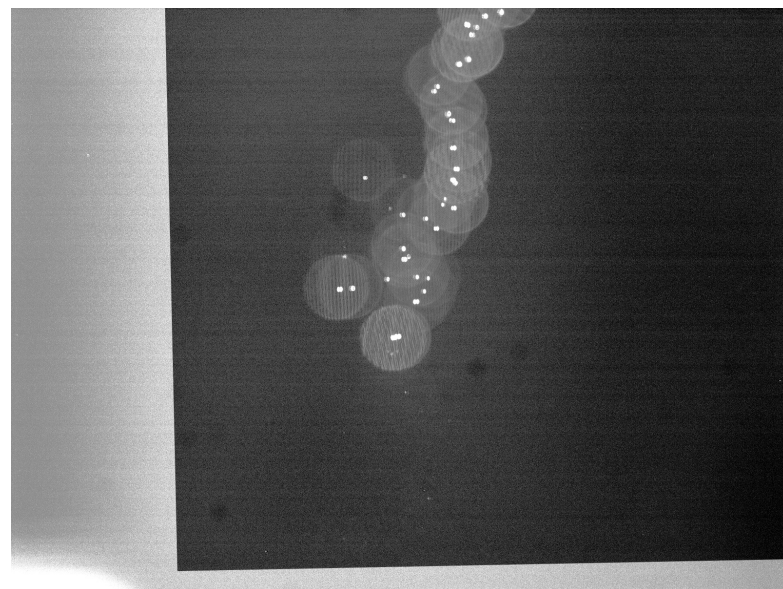
To correct for this error, we can use image registration techniques to derive the homography mapping *directly* from the focussed and defocussed droplet images, doing away with the need for calibration pictures altogether. Once we find the corrected homography

---

<sup>3</sup>Henceforth, the subscripts “foc” and “def” shall designate the focussed and defocussed cameras, respectively – even though both are focussed when the initial calibration photo is taken.



(a) Focussed camera image, after applying homography, is superimposed onto defocussed camera image of dot target plate.



(b) Focussed camera image, after applying homography derived from the calibration images, is superimposed onto defocussed camera image of droplets.

Figure 4.2: Illustration of the perspective error from misaligned calibration target plate

$\hat{\mathbf{H}}$ , we use it to find

$$\hat{\mathbf{P}}_{\text{def}} = \hat{\mathbf{H}} \mathbf{P}_{\text{foc}}, \quad (4.11)$$

which can be manually entered into the DynamicStudio software to replace  $\mathbf{P}_{\text{def}}$ .

### Finding the corrected homography

Image registration is the process of finding the best possible mapping of one image onto another – in other words, it is a term for homography-finding techniques. The basic process comprises three steps:

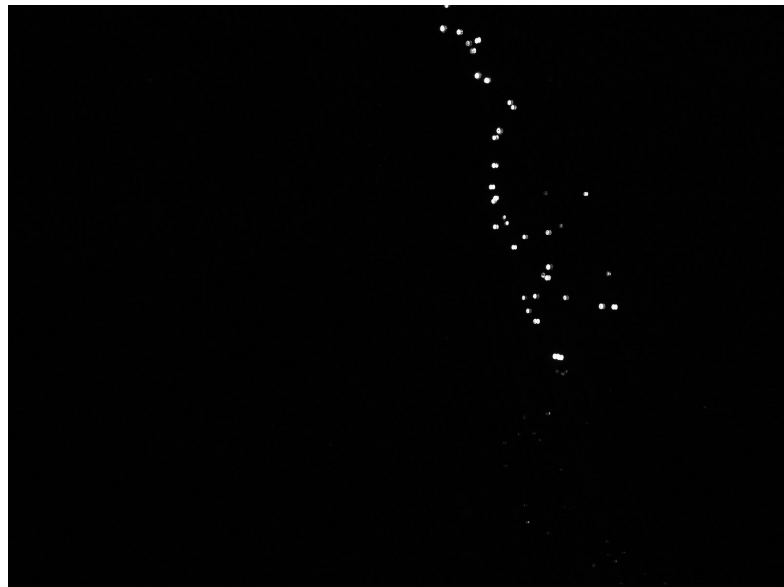
1. **Feature detection:** Finding “features”, i.e. unique points or regions in the images – such as corners, arcs, or contrasting regions which stay relatively stable even when the image is thresholded.
2. **Feature description:** Converting the detected features into numerical vectors.
3. **Feature matching:** Finding good correspondences between features in the two images – this often requires inlier/outlier decision-making, e.g. RANSAC.

Naturally, image registration is impossible to achieve between our focussed and defocussed images. We therefore first apply the following steps to our focussed image:

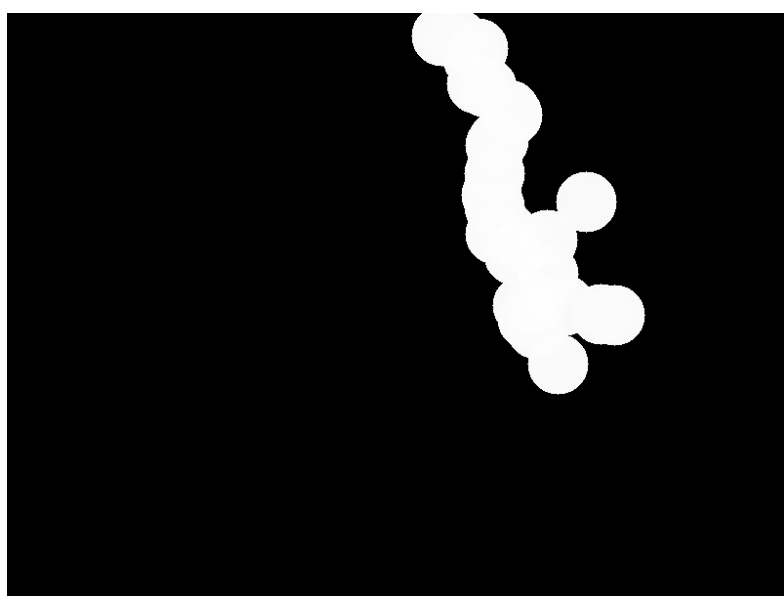
1. Mask the image, excluding all areas that are known not to contain droplets.
2. Subtract the pixel-wise minimum or mean taken over all images taken by the camera.  
This step will remove hot pixels on the camera’s CCD sensor and other static noise.
3. Erode the image, using a  $3 \times 3$  or  $5 \times 5$  kernel. This will close any remaining bright pixels which are likely noise.
4. Locate the intensity peaks in the remaining image.
5. Fill a new image with black, then draw white circles of diameter  $D_d$  onto it, centered at the respective positions of the intensity peaks detected in the focussed image.

The result of these operations is shown in Figure 4.3.

Image registration algorithms are often not very robust. This is especially true when the two pictures are not photos taken from slightly different angles. Moreover, image processing algorithms have runtime complexities that grow at least with the area of the image. We therefore prepare our focussed image by shrinking it to half the size (transformation  $\mathbf{S}_{0.5}$ ) and mirroring it horizontally (transformation  $\mathbf{M}_h$ ).



(a) Focussed camera image.



(b) Simulated defocussed camera image based on focussed camera image, used for registration.

Figure 4.3: Using the focussed image to simulate the defocussed image for registration

Our image registration algorithm makes use of the affine invariance of the ASIFT algorithm [1], but instead of the patented SIFT detector/descriptor pair [1], we use ORB [1] for feature detection and BRIEF [1] for feature description. A more detailed explanation of the algorithm can be found in Appendix ???. Figure 4.4 shows a successful mapping between focussed and defocussed images.

The homography found by the registration algorithm,  $\mathbf{K}$ , must now be converted into a homography between the original images,  $\hat{\mathbf{H}}$ . We see that

$$\mathbf{K} \mathbf{M}_h \mathbf{S}_{0.5} \mathbf{P}_{\text{foc}} = \mathbf{S}_{0.5} \mathbf{P}_{\text{def}}; \quad (4.12)$$

note here that the mirroring operation is applied only on one side of the equation, since the original images are mirrored and the goal is to undo this before running the image registration. To bring this into the form required by (4.10), we write

$$\mathbf{S}_{0.5}^{-1} \mathbf{K} \mathbf{M}_h \mathbf{S}_{0.5} \mathbf{P}_{\text{foc}} = \mathbf{S}_{0.5}^{-1} \mathbf{S}_{0.5} \mathbf{P}_{\text{def}} \quad (4.13)$$

$$= \mathbf{P}_{\text{def}} \quad (4.14)$$

Finally, it turns out that DynamicStudio violates convention by placing the coordinate origin at the bottom left corner of the image. We must therefore pre- and post-multiply by  $\mathbf{M}_v^{\pm 1}$  to arrive at our final expression for  $\hat{\mathbf{H}}$ :

$$\hat{\mathbf{H}} = \mathbf{M}_v \mathbf{S}_{0.5}^{-1} \mathbf{K} \mathbf{M}_h \mathbf{S}_{0.5} \mathbf{M}_v^{-1}. \quad (4.15)$$

We shall provide the transformation matrices for convenience:

$$\mathbf{M}_h = \begin{bmatrix} -1 & 0 & (\text{image width}) \\ 0 & 1 & 0 \\ 0 & 0 & 1 \end{bmatrix} \quad (4.16)$$

$$\mathbf{M}_v = \begin{bmatrix} 1 & 0 & 0 \\ 0 & -1 & (\text{image height}) \\ 0 & 0 & 1 \end{bmatrix} \quad (4.17)$$

$$\mathbf{S}_{0.5} = \begin{bmatrix} 0.5 & 0 & 0 \\ 0 & 0.5 & 0 \\ 0 & 0 & 1 \end{bmatrix} \quad (4.18)$$

The improved matching achieved using  $\hat{\mathbf{P}}_{\text{def}}$  is shown in Figure 4.5. Having calculated  $\hat{\mathbf{P}}_{\text{def}}$  using equation (4.11), we can import it into DynamicStudio to improve the identifica-

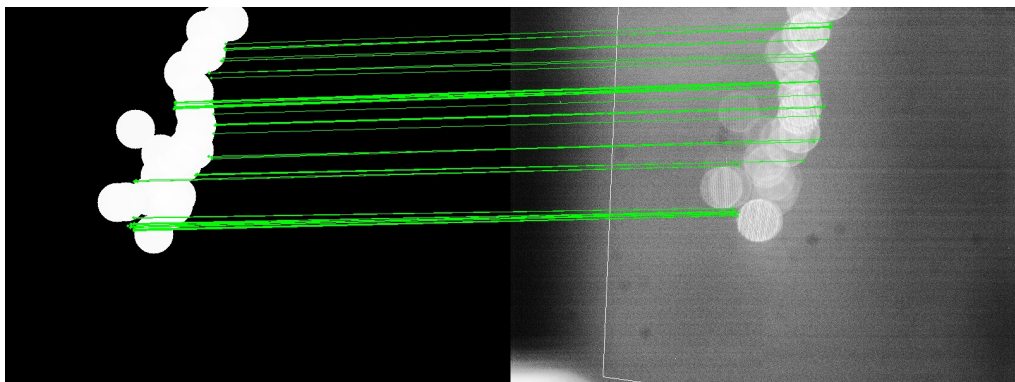


Figure 4.4: Matching between focussed and defocussed images.

tion of droplets.

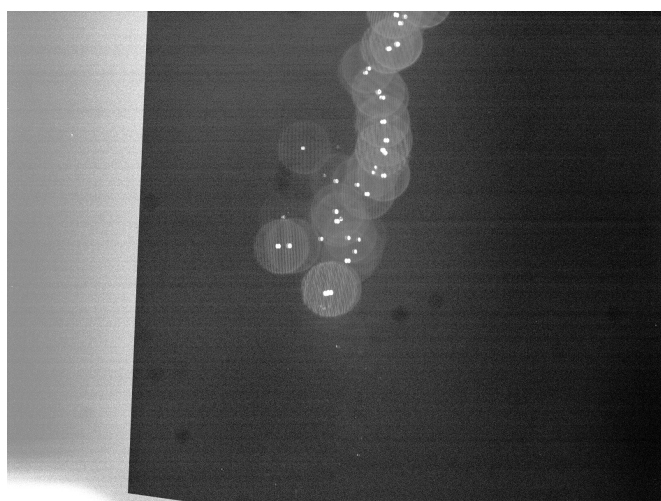


Figure 4.5: Focussed camera image, after applying homography derived from image registration, is superimposed onto defocussed camera image of droplets.

# Particle sizing with a slit aperture

As we discussed in Section 4.3.1, many otherwise well-executed IPI measurements are thwarted by overlapping defocussed droplet images. This problem is never more apparent than in efforts to calibrate the system using a vibrating orifice droplet generator, as the droplets produced thereby are spaced very closely and produce heavily overlapping defocussed images. Fortunately, there exists a simple and reliable technique to deal with this problem: a slit aperture, installed directly in front of the lens, masks the defocussed droplet images such that only a thin strip across their center passes through the lens. The effect is shown in Figure 5.1.

The idea of optically compressing an image in one direction is well-known from the field of spectroscopy. It was first introduced to the area of fluid measurement by Durst et al. [29], and has since been employed in various forms, e.g. by Pan et al. [24]. Other authors use cylindrical lenses instead of slit apertures to achieve the vertical integration of the image [26].

## 5.1 The slit aperture

Naturally, equations (4.2) and (4.3) still hold.

(Insert a diagram of the setup)

(Describe how an aperture can be created in any lab)

(Show a picture of the lens with aperture)

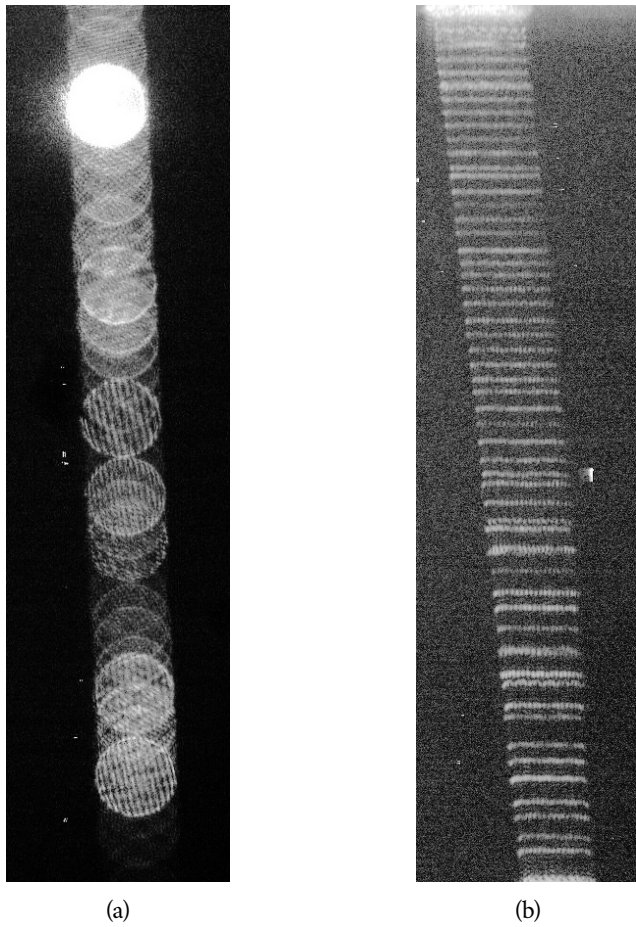


Figure 5.1: Before (a) and after (b) installing the slit aperture. The aperture stop pares off the top and bottom halves of the defocussed circles, leaving only a narrow center string in the middle.

## 5.2 Image processing

Extracting the fringe counts from such an image is straightforward. First, we correlate the image with that of a single, solid bright rectangle which shares the approximate dimensions of a typical strip in the image. This operation yields intensity peaks centered over our regions of interest. We remove closely adjacent peaks, as they may represent questionable or overlapping strips. Compared to the sheer number of correctly identified strips, the number of legitimate data points lost this way is negligible. Figure 5.2 shows the result of such an attempt at identifying the strips.

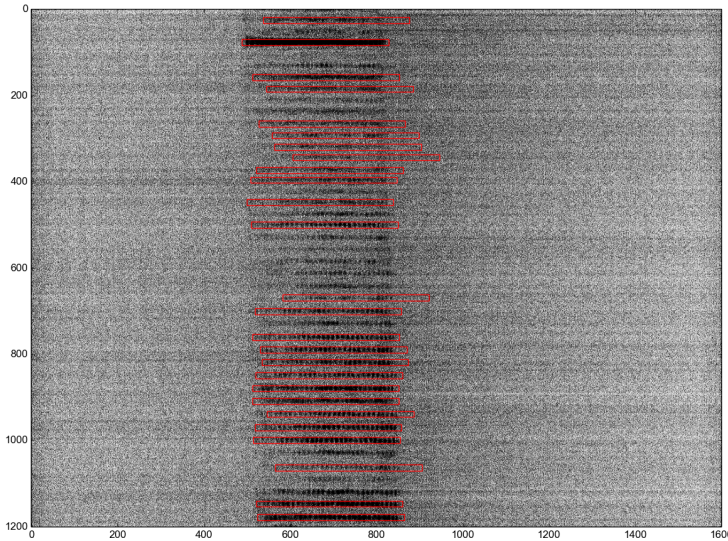


Figure 5.2: The image is correlated with that of a solid bright rectangle, which results in peaks that approximately coincide with the centres of the strips. Here, the original photo is shown with rectangles drawn centered at said peaks.

To find the number of fringes within the strip, we cannot rely on counting the number of dark/bright variations directly, as some of them may be lost in the noise. The spatial frequency of the peaks, however, taken together with the known and constant horizontal width of the strips, will produce a reliable fringe count. In the next step, our algorithm therefore applies the Fourier transform to each region of interest. To improve the accuracy of the method, three steps are performed before the Fourier transform is taken:

1. a weak ( $3 \times 3$ ) Gaussian blur is applied to the region (optional);
2. a Hanning window is applied to the region – both horizontally and vertically. This reduces the “sinc ringing” effect encountered when taking the Fourier transform of finite signals;
3. the region is padded with zeros in all directions to yield a larger input to the Fourier transform. In our application, the windowed and padded strip images had dimensions of  $1024 \times 1024$  pixels. Zero-padding increases the granularity of the frequency spectrum, which can help with the correct identification of the peak frequency.

Figure 5.3 shows the windowed appearance of one such region of interest (although it does not show the padded input to the Fourier transform due to space constraints). The Fourier transform yields a frequency power spectrum in two dimensions, although we are

primarily interested in the frequency peak in the horizontal direction (i.e. along  $y = 0$ ). In order to minimize the misidentification of dominant frequencies,

1. we clip the spectrum to a band of reasonable frequencies. This is necessary because a)  $1/f$ -noise causes very low frequencies to dominate in power, although they are of no interest to us, and b) graininess in the original photo can sometimes result in meritless high-frequency peaks;
2. we apply a Gaussian blur to the 2D spectrum to remove outliers in the spectrum;
3. we discard all regions in which the peak frequency's power does not exceed a certain value;
4. we discard all regions in which the *prominence* of the peak frequency's power (i.e. its proportion to the mean power) does not exceed a certain value (this step is optional).

The bottom two elements in Figure 5.3 illustrate the effect of these steps.

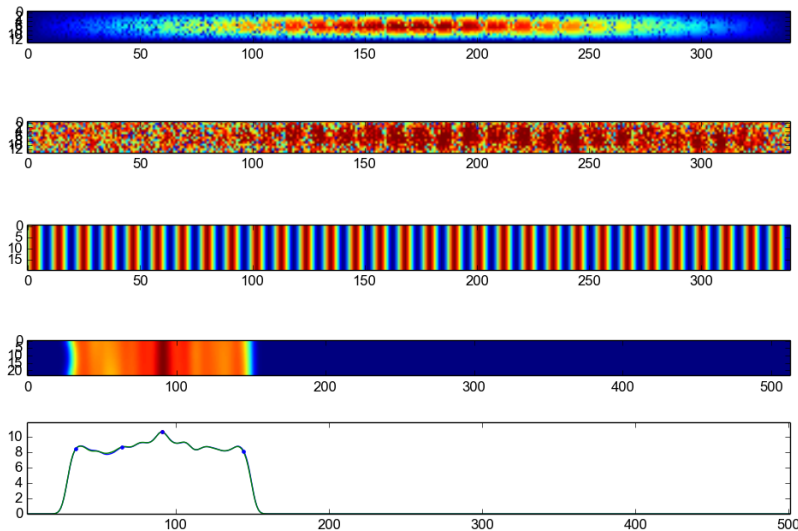


Figure 5.3: From top to bottom: windowed region of interest; original (unwindowed) region of interest; sine wave representing the identified peak frequency; clipped and lowpass-filtered 2D frequency spectrum showing a distinct peak at about 90 oscillations across the image width of 1024 pixels; 1D plot of the frequency spectrum, with peak identified at  $f = 91.0$ .

Finally, the peak frequency  $f_{\text{peak}}$  is converted into a fringe count by re-scaling it from the padded size  $D_{\text{padded}}$  ( $= 1024$  pixels) to the width of the strip (which, in the context of

IPI measurements, should equal the diameter  $D_i$  of the defocussed droplet image):

$$N_{fr} = f_{peak} \frac{D_i}{D_{padded}} \quad (5.1)$$

In the current implementation of our algorithm,  $D_i$  must be determined and entered manually.

## 5.3 Sources of error with the slit method

### 5.3.1 Misalignment of slit and lens

While the above algorithm will generally give a good estimate of the fringe

count for a given defocussed droplet image, it cannot know whether the entire center portion of the image has indeed passed the slit aperture. It is conceivable, after all, that the slit aperture was not perfectly centered on the lens entrance, or that the slit aperture was shorter than the diameter of the lens entrance. Figure 5.4 illustrates how the slit aperture can cause the defocussed image to appear smaller than it is. The reduced value for  $D_i$ , manually entered in equation (5.1), will result in droplets being reported as smaller than they are in reality.

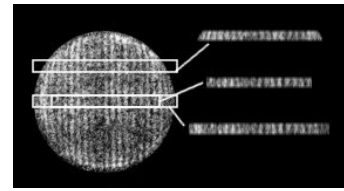


Figure 5.4: Only a slit aperture centered on the lens and extending across the entire lens entrance will preserve all fringes

## 5.4 Calibrating the slit method

Taking into account the sources of errors explained in the sections above, it is advisable to run a few calibration tests with droplets of different sizes before employing the IPI technique for real spray measurements. Recall that, if we ignore the Mie error (Section 4.3.3), the relationship between fringe count and droplet diameter is linear with a constant of proportionality  $\alpha$  (see equation (4.2)). The aim of our calibration, then, is to determine the value of  $\alpha$  from experiment – the premise being that we cannot be certain of the values of  $D_a$ ,  $z$ , and possibly not even  $m$  and  $\varphi$  (although the latter can usually be ascertained to a sufficient degree of accuracy).

### 5.4.1 A sample calibration of the slit aperture method

Using the droplet generator described in Section 3 and the IPI configuration described in Section 4.2, we produced and measured monodisperse droplets of many different diameters. The droplet diameters were determined both mathematically and photographically, as described in Section ???. Out of over 30 sets of IPI measurements we selected six sets that exhibited both strong uniformity and high photographic quality:

Set	Flow rate	Frequency	$D_d$ , predicted	$D_d$ , from photo	$\hat{N}_{fr}$
FA	20.8 ml/h	5395 Hz	127 $\mu\text{m}$	126 $\mu\text{m}$	9.71
FB	39.7 ml/h	1990 Hz	220 $\mu\text{m}$	226 $\mu\text{m}$	16.71
FC	79.4 ml/h	1565 Hz	299 $\mu\text{m}$	291 $\mu\text{m}$	22.92
FD	94.3 ml/h	1067 Hz	361 $\mu\text{m}$	367 $\mu\text{m}$	27.26
FE	114.1 ml/h	1065 Hz	384 $\mu\text{m}$	384 $\mu\text{m}$	29.89
FF	175.2 ml/h	1038 Hz	447 $\mu\text{m}$	454 $\mu\text{m}$	34.56

Table 5.1: Six sets of calibration data taken with the setup described in Section 4.2

The values for  $\hat{N}_{fr}$ , the peak fringe count, are based on the histograms (see Figure 5.5) showing the distribution of fringe counts within each dataset. These fringe counts are of course found by the algorithm described in Section 5.2.

It is worthwhile to point out some apparent idiosyncrasies in the histograms of datasets FB and FC. Their peak fringe counts are 16.71 and 22.92, but there are secondary peaks at about 21 and 29 fringes, respectively. The latter are explained by the collision of droplets as discussed in Section 3.4.1, and are ignored for the purposes of calibration.

The close agreement of the droplet diameters found from photographs with those predicted by (??) reassures us that we can use the predicted  $D_d$  for further analysis.

At this point, we can least-squares-fit the linear relationship (4.2) to the primary peaks  $\hat{N}_{fr}$  and the known droplet diameters  $D_d$  to find  $\hat{x}$ :

$$\hat{x} = \frac{\sum_i D_{d,i} \hat{N}_{fr,i}}{\sum_i D_{d,i}^2} \quad (5.2)$$

Note that instead of the standard least squares regression we here use a simplified formula to force the trend line through the origin. This choice should not be made lightly, since it will usually cause the residuals to have a non-zero mean. In this case, however, we believe it to be justified to require that  $D_d = 0$  for  $N_{fr} = 0$ .

Based on the values in Table 5.1, we thus arrive at a value of  $\hat{x} = 76808.1$  with an  $R^2$ -value of 99.98%.

### 5.4.2 Discussion

Figure 5.6 illustrates the good agreement on  $\chi$  between all datasets. Considering the sheer number of error sources – from the unavoidable non-uniformity of the generated droplets to the uncertainty that comes with taking the Fourier transform of a noisy image – the calibration results documented here are a testament to the practical robustness of the method.

It must be remembered, of course, that the peak fringe count values  $\hat{N}_{\text{fr}}$  forming the basis of our calculation are taken from the peaks of Gaussians fitted to the raw fringe count histograms (see Figure 5.5). In other words, it is our assumption that all droplets from a given dataset produce fringe counts that are normally distributed around their respective  $\hat{N}_{\text{fr}}$ . The histogram to dataset FA shows a much higher deviation than the others – this may be due to genuine variance in the generated droplet diameters or to difficulty in processing comparatively weak images with low fringe counts. It seems likely that both effects contribute.

We can compare the empirically determined value  $\hat{\chi}$  with the mathematical result obtained from (4.2). Substituting  $\lambda = 532 \text{ nm}$ ,  $m = 1.3324$  and  $\varphi = 90^\circ$ , we conclude that

$$\frac{D_a}{z} = 2 \sin \left( \frac{\hat{\chi} \lambda}{\cos \frac{\varphi}{2} - \frac{m \sin \frac{\varphi}{2}}{\sqrt{m^2 + 1 - 2m \cos \frac{\varphi}{2}}}} \right) = 2 \sin(3.11982 \cdot 10^{-7} \hat{\chi}) \quad (5.3)$$

so for  $\hat{\chi} = 76808.1$ ,  $\frac{D_a}{z} = 0.047921$ . Recall that this quotient is a measure of the collection angle and closely related to the numerical aperture  $\text{NA} = \sin \frac{D_a}{2z}$ . If needed, we can now use this result to compute the input parameters  $D_a$  and  $z$  in the DantecStudio IPI software: given, for instance,  $z = 45.0 \text{ cm}$ , we can obtain the entrance pupil diameter as

$$0.047921 \cdot 450 \text{ mm} = 2.156 \text{ mm} \quad (5.4)$$

## 5.5 Conclusion

- It's impossible to calibrate IPI using a VOAG
- The slit aperture works pretty well
- Calibration is easy, and one or two calibrations are probably enough
- A good collection angle (i.e. camera-laser distance) must be chosen

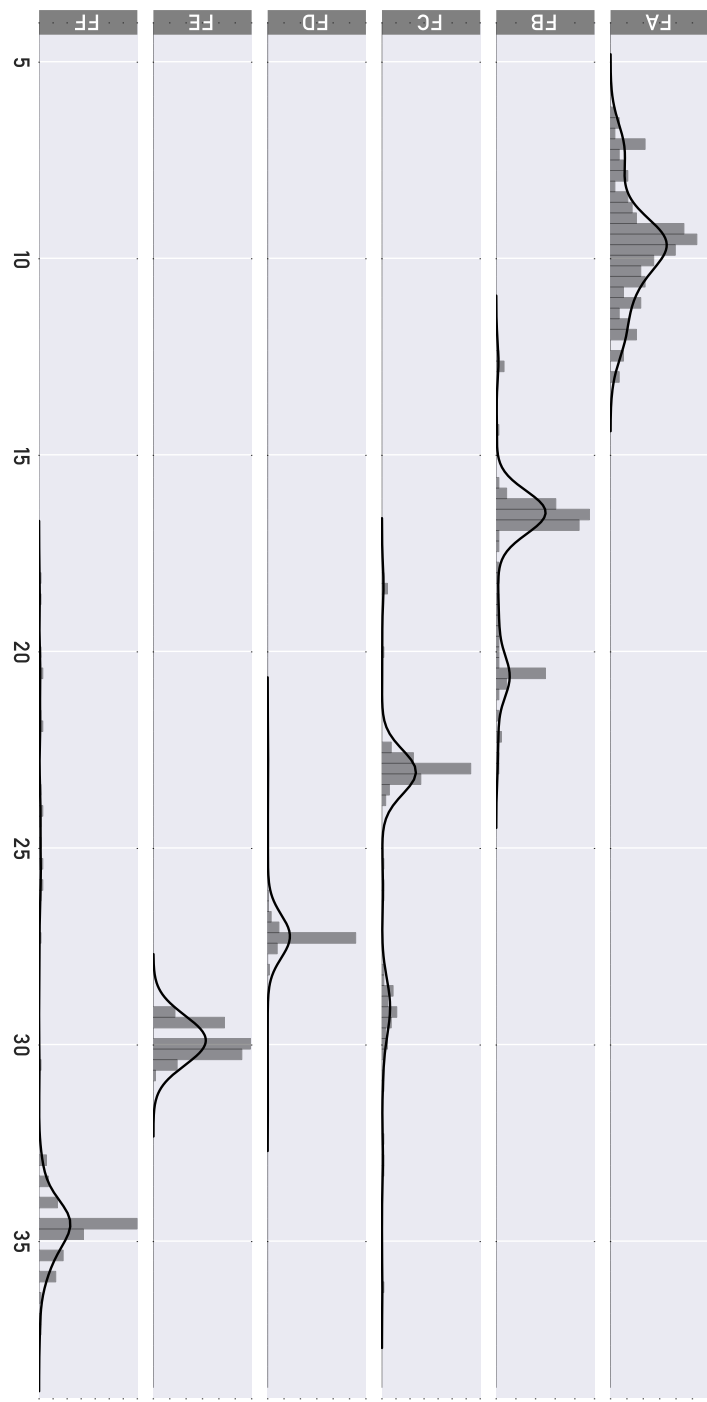


Figure 5.5: Normalized distributions of measured fringe counts  $N_f$  for the six datasets listed in Table 5.1. Solid lines are Gaussian kernel density estimates with  $h = 0.5$ .

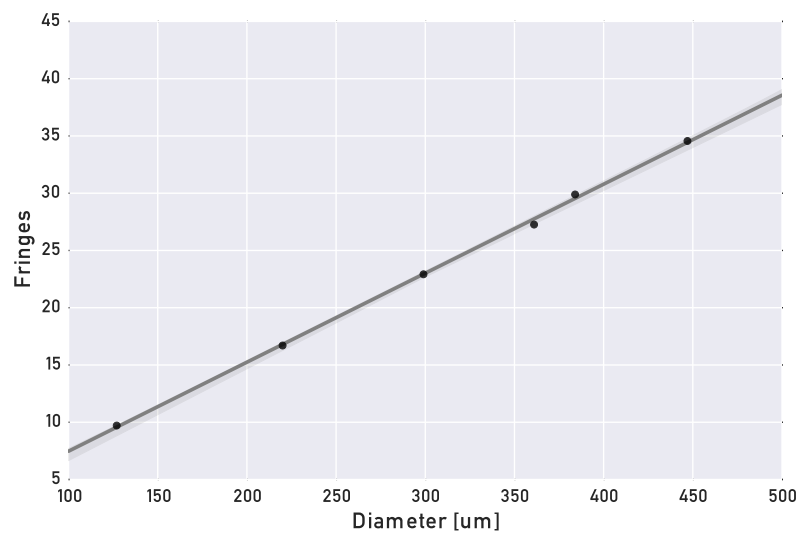


Figure 5.6: Scatterplot of Table 5.1 showing the peak fringe counts  $\hat{N}_{fr}$  for each predicted droplet diameter  $D_d$



# Phase-Doppler Particle Analysis (PDPA)

## 6.1 Optical principle

(Explanation)

## 6.2 Sources of error

### 6.2.1 Gaussian beam divergence

The theory predicting the linear relationship between detector phase difference and droplet diameter is founded on the assumption of very small droplets and plane beam wavefronts.  
**(Question: is it the wavefront curvature or the non-uniformity of the intensity that causes problems?)**

The problem is termed *trajectory ambiguity effect* (TAE) or *Gaussian beam defect* (GBD) in the literature.

This phenomenon was recognized first by Saffman [30] but had to be neglected until the plane-wave scattering theory of Lorenz-Mie optics was extended into the *Generalized Lorenz-Mie Theory* (GLMT). Most of this work was done by Gouesbet, Gréhan, Maheu, Lock and others throughout the 1980s [31, 32, 33, 34], and mathematically rigorous formulations were available by the early 1990s [35, 36]. The 1996 paper by Gouesbet and Gréhan summarizes these developments and provides an early overview over the attempts to circumvent the TAE [37]. More discussion is given e.g. by

Solutions are a) a planar setup, b) double-burst measurements, c) epsilon validity mea-

surements. It is important to align the receiver properly; the tables used by TSI were developed using GLMT by Naqwi and Menon [38].

#### 6.2.2 Slit effect

Durst et al show experimentally that the slit effect is even more crucial than the Gaussian beam effect. [29]. Together with the TAE, this is called the measurement volume effect. Qiu and Hsu propose using four detectors, instead of three, to resolve this problem entirely [39]. A similar design was verified experimentally by Sipperley and Bachalo [40].

A more recent review of the phenomenon and associated techniques was given by Strakey et al. [41? ].

#### 6.2.3 Change in fringe frequency over $z$

The curved wavefront causes the fringe spacing to vary along the axis of the measurement volume. At the near and far ends of the volume, the fringes are spaced wider, which can result in an error on the order of 10%. (Red Book)

#### 6.2.4 Selection of lenses and masks

Davis and Disimile talk about the TAE only tangentially. They provide results of the same spray using different masks and focal lengths [42].

#### 6.2.5 Optical aberrations

See Dressler and Kraemer [21].

#### 6.2.6 Wrongly entered parameters

The optical principle involves many more geometric parameters than are needed for the operation of IPI or laser diffraction (Malvern) devices. As a result, an excellent interface and a very attentive user are required to ensure accurate results.

In practice, I always get error messages when doing the last step, and the values are way out of the expected range. The result, then, is that the D20 is made very close to the expected monodisperse diameter. Since the D20 is quite a bit larger than the actual (and completely obvious) peak value, even these "wrong" values aren't correct.

## 6.3 Calibration

Calibration is tricky, because

```
knowndiam = argmax(gaussian(average(diamAB[within7percent], diamAC[within7percent])))
```

Since the selection of droplets with  $<=\text{diff}(\text{diam})$  and the gaussian kernel density estimate are one-way functions, it's impossible to work backwards. We also want to minimize the angle in the difference-diameter plot, i.e. the PCA is supposed to be as close as possible to 0 and 90 degrees. So the only way to do this reliably is to iterate over the two AB and AC values to find an optimum.

Nonetheless, even with this method the relationship between the distance values AB and AC is typically linear, and once the linear relationship has been found, we can find the combination of values that produces the most straight PCA and the most centered cluster. Let's approximate the



# Bibliography

- [1] W. H. Walton and W. C. Prewett. The production of sprays and mists of uniform drop size by means of spinning disc type sprayers. *Proceedings of the Physical Society B*, 62: 341–350, Jun 1949.
- [2] C. R. Merritt and J. A. Drinkwater. A laboratory device for producing single drops in uniform sizes of 150–450  $\mu\text{m}$  diameter. *Pesticide Science*, 8:457–562, 1977.
- [3] C. R. Allan, H. R. Carlon, A. K. Stuempfle, T. E. Hoffer, and R. L. Pittier. Survey of the literature: Controlled generation of liquid droplets. Technical Report TR-88164, Chemical Research, Development & Engineering Center, U.S. Army Munitions Chemical Command, Aug 1988.
- [4] W. R. Lane. A microburette for producing small liquid drops of known size. *Journal of Scientific Instruments*, 24:98, Apr 1947.
- [5] K. Reil and J. Hallett. An apparatus for the production of uniform sized water drops, at desired time intervals. *Review of Scientific Instruments*, 40:533–534, Apr 1969.
- [6] S. Coggins and E. A. Baker. Micro sprayers for the laboratory application of pesticides. *Annals of Applied Biology*, 102:149–154, Feb 1983.
- [7] W. J. Stry. *The combustion of free flowing droplets of chlorinated benzenes, alkanes, and their mixtures*. PhD thesis, SUNY Buffalo, September 1992.
- [8] I. Endo, Y. Sato, S. Saito, T. Nakagiri, and S. Ohno. Bubble jet recording method and apparatus in which a heating element generates bubbles in a liquid flow path to project droplets, February 2 1988. US Patent 4,723,129.
- [9] A. V. Sergeyev and R. A. Shaw. An inexpensive uniform-size aerosol generator. *Measurement Science and Technology*, 17:N41, 2006.

- [10] J. C. Yang, W. Chien, M. King, and W. L. Grosshandler. A simple piezoelectric droplet generator. *Experiments in Fluids*, 23:445–447, 1997.
- [11] H. Ulmke, T. Wriedt, and K. Bauckhage. Piezoelektrischer Tropfengenerator zur Kalibrierung von Partikelzählern. *Chemie Ingenieur Technik*, 71(12):1387–1391, 1999.
- [12] H. P. Le. *Progress and trends in inkjet printing technology*, volume 42.
- [13] E. Lee. *Microdrop Generation*. Nano- and Microscience, Engineering, Technology and Medicine. Taylor & Francis, 2002.
- [14] A. Amirzadeh Goghari and S. Chandra. Producing droplets smaller than the nozzle diameter by using a pneumatic drop-on-demand droplet generator. *Experiments in Fluids*, 44:105–114, Jan 2008.
- [15] G. J. Green, D. E. Walsh, F. Takahashi, and F. L. Dryer. Aerodynamic device for generating mono-disperse fuel droplets. *Review of Scientific Instruments (ISSN 0034-6748)*, 60:646–652, Apr 1989.
- [16] F. Savart. Memoire sur la constitution des veines liquides lancees par des orifices circulaires en mince paroi. *Annales de Chimie et de Physique*, 53:337–386, 1833.
- [17] L. Rayleigh. On the capillary phenomena of jets. *Proceedings of the Royal Society of London*, 29:71–97, 1879.
- [18] R. J. Donnelly and W. Glaberson. Experiments on the capillary instability of a liquid jet. *Proceedings of the Royal Society of London. Series A. Mathematical and Physical Sciences*, 290(1423):547–556, 1966. doi: 10.1098/rspa.1966.0069.
- [19] J. M. Schneider and C. D. Hendricks. Source of uniform-sized liquid droplets. *Review of Scientific Instruments*, 35:1349–1350, Oct 1964.
- [20] R. N. Berglund and B. Y. H. Liu. Generation of monodisperse aerosol standards. *Environmental Science and Technology*, 7:147–153, Feb 1973.
- [21] J. L. Dressler and G. O. Kraemer. A multiple drop-size drop generator for calibration of a phase-doppler particle analyzer. *Liquid Particle Size Measurement Techniques*, 2 (1083):30–44, 1990.
- [22] L. Ström. The generation of monodisperse aerosols by means of a disintegrated jet of liquid. *Review of Scientific Instruments*, 40:778–782, Jun 1969.

- [23] A. R. Glover, S. M. Skippon, and R. D. Boyle. Interferometric laser imaging for droplet sizing: a method for droplet-size measurement in sparse spray systems. *Appl Opt*, 34: 8409–8421, Dec 1995.
- [24] G. Pan, J. Shakal, W. Lai, R. Calabria, P. Massoli, and O. Pust. Simultaneous global size and velocity measurement of droplets and sprays. *Spray '06 – Workshop über Sprays, Erfassung von Sprühvorgängen und Techniken der Fluidzerstäubung*, 2006.
- [25] H. van de Hulst. *Light Scattering by Small Particles*. Dover Books on Physics. Dover Publications, 2012.
- [26] T. Kawaguchi, Y. Akasaka, and M. Maeda. Size measurements of droplets and bubbles by advanced interferometric laser imaging technique. *Meas Sci Technol*, 13:308–316, Feb 2002.
- [27] C. Mounaïm-Rousselle and O. Pajot. Droplet sizing by mie scattering interferometry in a spark ignition engine. *Part Part Syst Charact*, 16:160–168, 1999.
- [28] N. Damaschke, H. Nobach, and C. Tropea. Optical limits of particle concentration for multi-dimensional particle sizing techniques in fluid mechanics. *Experiments in Fluids*, 32:143–152, 2002.
- [29] F. Durst, C. Tropea, and T.-H. Xu. The slit effect in phase doppler anemometry. In *Modern techniques and measurements in fluid flows: Proceedings of the 2nd International Conference on Fluid Dynamic Measurement and Its Applications*, Oct 1994.
- [30] M. Saffman. The use of polarized light for optical particle sizing. In *Proceedings of the 3<sup>rd</sup> International Symposium on Applications of Laser Anemometry to Fluid Mechanics, Lisbon, Portugal*, page 18.2, 1986.
- [31] G. Gréhan, G. Gouesbet, and C. Rabasse. The computer program supermidi for lorenz-mie theory and the research of one-to-one relationships for particle sizing. In *Proceedings of the symposium on long range and short range optical velocity measurements*, Institut franco-allemand de Saint-Louis, September 1980.
- [32] G. Gouesbet and G. Gréhan. Sur la généralisation de la théorie de lorenz-mie. *Journal of Optics*, 13(2):97–103, 1982.
- [33] G. Gouesbet, B. Maheu, and G. Gréhan. Light scattering from a sphere arbitrarily located in a gaussian beam, using a bromwich formulation. *Journal of the Optical Society of America A*, 5(9):1427–1443, 1988.

- [34] B. Maheu, G. Gouesbet, and G. Gréhan. A concise presentation of the generalized lorenz-mie theory for arbitrary location of the scatterer in an arbitrary incident profile. *Journal of Optics*, 19(2):59–67, 1988.
- [35] J. A. Lock and G. Gouesbet. A rigorous justification of the localized approximation to the beam shape coefficients in generalized lorenz-mie theory, i. on-axis beams. *Journal of the Optical Society of America A*, 11(9):2503–2515, 1994.
- [36] G. Gouesbet and J. A. Lock. A rigorous justification of the localized approximation to the beam shape coefficients in generalized lorenz-mie theory, ii. off-axis beams. *Journal of the Optical Society of America A*, 11(9):2516–2525, 1994.
- [37] G. Gouesbet and G. Gréhan. Gaussian beam errors in phase-doppler anemometry and their elimination. In R. Adrian, D. Durão, F. Durst, M. Heitor, M. Maeda, and J. Whitelaw, editors, *Developments in Laser Techniques and Applications to Fluid Mechanics*, pages 243–259. Springer Berlin Heidelberg, 1996.
- [38] A. Naqwi and R. Menon. A rigorous procedure for design and response determination of phase doppler systems. In *Proceedings of the 7<sup>th</sup> International Symposium on Applications of Laser Anemometry to Fluid Mechanics, Lisbon, Portugal*, pages 340–353, 1994.
- [39] H. Qiu and C. T. Hsu. Method of phase-doppler anemometry free from the measurement-volume effect. *Applied Optics*, 38(13):2737–2742, May 1999.
- [40] C. M. Sipperley and W. D. Bachalo. Triple interval phase doppler interferometry: Improved dense sprays measurements and enhanced phase discrimination. In *17th International Symposium on Applications of Laser Techniques to Fluid Mechanics, Lisbon, Portugal*, Jul 2014.
- [41] P. A. Strakey, D. G. Talley, S. V. Sankar, and W. D. Bachalo. Phase Doppler Interferometry with Probe-to-Droplet Size Ratios Less Than Unity. Part I: Trajectory Errors. *Applied Optics*, 39(22):3875–3886, Aug 2000.
- [42] J. M. Davis and P. J. Disimile. The effect of optical configuration selection on phase doppler anemometer fire suppressant nozzle characterizations. In *14th Halon Options Technical Working Conference*, May 2004.